Diffusion-driven formation of Co_3O_4 nanopetals layers for photoelectrochemical degradation of organophosphate pesticides

B. Kalinic[a], L. Girardi[b], P. Ragonese[a], A. Faramawy[a], G. Mattei[a], M. Frasconi[b,*], R. Baretta[b], S. Bogialli[b], M. Roverso[b], G.A. Rizzi[c], C. Maurizio[a,*]

[a] *Physics and Astronomy Department and CNISM, University of Padova, via Marzolo 8, I-35131 Padova, Italy*
[b] *Department of Chemical Sciences, University of Padova, via Marzolo 1, 35131 Padova, Italy*
[c] *CNR-ICMATE and INSTM,Department of Chemical Sciences, University of Padova, via Marzolo 1, 35131 Padova, Italy*

Abstract

A new light is shed on the formation mechanism of Co_3O_4 nanopetals on Si-based photoanodes by thermal oxidation of a deposited metallic film, and on their use for the rapid chemisorption, the photoelectrochemical detection and subsequent removal of harmful fenitrothion (FNT), a commonly used organophosphate pesticide which represents a serious risk to the public health. Using Au clusters as markers for the external surface of the as-deposited film, the results of complementary experiments indicate that the Co_3O_4 petal formation during oxidizing annealing is related to the non-uniform Co out-diffusion and oxidation rather than to a local melting, as previously suggested. When grown on Si photoanodes under controlled conditions, Co_3O_4 nanopetals are stable and exhibit high photoelectrocatalytic activity due to the increased active area with respect to the corresponding thin film. These nanostructures work efficiently for FNT sensing (sensitivity of 0.1 $\mu A/(cm^2 \mu M)$) through the direct coordination of the FNT nitro-groups on the Co(II) centers, that inhibit the Co(II) oxidation. Furthermore, we demonstrate that a low amount of this nanostructured film, polarized at a modest bias (1.45 V vs RHE) and under visible light illumination (100 mW/cm^2), can efficiently remove the pesticide in water with a time constant of 1 h without the need for catalyst recollection, and remains stable, thus making it suitable for environmental remediation applications.

Keywords: transition metal oxide nanostructures, photoelectrocatalysis, Co_3O_4 nanopetals, nanostructure growth, FNT degradation, organophosphate pesticides

*Corresponding authors
Email addresses: marco.frasconi@unipd.it (M. Frasconi), chiara.maurizio@unipd.it (C. Maurizio)

April 19, 2022

1. Introduction

Organophosphate (OP) compounds are widely used as persistent pesticides in agriculture. Their occurrence in the environment, especially water resources, is raising concerns because of the negative effects on human health, even at very low concentrations [1]. Therefore, great efforts have been made to develop methods for monitoring their presence in the environment and removing them in order to mitigate the effects of contamination [2, 3]. Owing to the exceptional catalytic properties and to the large surface-to-volume ratios, catalysts in form of nanostructured materials have attracted substantial attention for the development of sensitive sensors for the detection of OP compounds [4, 5] and for the removal of pesticides and organic pollutants by adsorption [3] or photodegradation mechanisms with the formation of less harmful by-products [6, 7, 8, 9, 10, 11]. For example, trace level detection of fenitrothion (FNT), a commonly used organophosphate pesticide, was obtained by 3D flower-like gadolinium molybdate catalyst, which was also employed, in form of dispersed nanopowder, for the high efficiency FNT removal in water [12]. The photodegradation of pesticides often relies on the use of the catalyst suspended in water, which raises another potential problem on the catalyst removal after use. Therefore, suitable catalysts in form of nanostructured materials tightly anchored to solid substrates would be an ideal platform for the development of novel approaches for the selective detection and degradation of OP compounds. For example semiconductor photocatalysts, such as N-WO_3/Ce_2S_3 nanotube bundles, has been synthetized on carbon textile supports resulting in a robust and highly efficient photocatalysts for the photocatalytic degradation of phenol [11]. The effectiveness of photocatalysts supported on a solid substrate can be easily further powered by the application of an electrochemical potential, while to evaluate the global efficiency, the amount of used catalyst should also be taken into account. The development of a chemically and mechanically stable nanostructured system of this kind would pave the way towards efficient procedures for photo-assisted pesticide degradation with no need for regeneration and that could easily become more economically viable.

Co_3O_4 in form of nanostructured thin films has been widely investigated [13], with recent works dealing with applications as supercapacitors [14] and sensors [15, 16, 17, 18] as well as with its superior catalytic and photocatalytic performances [19, 20], coupled to a protective action towards Si photoanodes for water splitting applications [21, 22]. Co_3O_4 films decorated with nanopetals and nanowalls combine a wide surface area with a robust structure, interesting for photoelectrocatalytic applications in oxygen evolution reactions or photoelectrochemical sensing [23, 21]. The formation of a nanopetal layer can be obtained by oxidation of a metallic Co foil or film in the temperature range 300-450°C [24, 25, 26, 27]. Despite the relatively easiness of the preparation procedure, the

mechanism at the basis of the nanopetal formation is still debated in literature. It has been suggested that the formation process is a sort of Solid-Liquid-Solid (SLS) process, involving the melting and successive re-crystallization of a thin Co or Co-oxide surface layer [28, 24, 27, 26]. Nevertheless, it has to be considered that the bulk melting temperature of Co is 1495 °C and those of the corresponding oxides (CoO, Co_3O_4) is even higher, making the SLS process unlikely. Moreover, it can be expected that the diffusion of vacancies, that at high temperature is responsible for the oxidation kinetics of bulk Co [29], can play an important role even at moderate temperature, when nanostructures are concerned [30, 31].

In this paper we shed new light on the formation process of Co_3O_4 nanopetals as a consequence of an oxidizing annealing of a thin Co film obtained by Physical Vapor Deposition (PVD) with thickness in the range 20-200 nm. A combined morphological and structural analysis of the nanostructured films after specific annealing conditions shows that the petal formation is a mechanism induced by out-diffusion of Co from the original film surface and on its subsequent oxidation. The presented results clarify that the petal formation requires a finely controlled equilibrium between the oxygen diffusion into the film and the non-uniform out-diffusion of Co from the metallic film. We show that the generation of well-developed Co_3O_4 nanopetals on n-Si substrates allows the rapid photoelectrochemical detection and subsequent efficient degradation of fenitrothion (FNT), which has been chosen as a model organophosphate pesticide. The detection of this organophosphorus compound by the Co_3O_4 nanopetals on n-Si relies on the unprecedented and rapid chemisorption of the FNT nitro-group on Co(II) surface sites that leads, upon visible light illumination, to a decrease in the photocurrent density, resulting in an easy detection of the pesticide. The sensor achieves good analytical characteristics such as sensitivity and linear range for the detection of FNT, with no loss in performance over time, also owing to the overall structural robustness of the nanopetals. Finally, the concomitant production of hydroxyl radicals that occurs during the water splitting process on the Co_3O_4 nanopetals leads to an efficient decomposition of FNT under visible light exposure and even at moderate bias application (1.45 V vs RHE). This is achieved using a small amount of catalyst anchored on a solid substrate. Considering the much lower supply risk for cobalt with respect to other catalysts as those based on rare-earths [32], these findings demonstrate the many advantages of Co_3O_4 nanopetal layers on Si for the photoelectrochemical sensing and degradation organophosphorus pesticides, with reproducibility, sensitivity, long term stability, and cost-effectiveness, that make this material highly amenable to field applications.

2. Experimental

Preliminary to the Co deposition, the substrates were cleaned using a piranha solution H_2SO_4:H_2O_2 3:1 for 1 hour at 60 °C. Co films were deposited on Si and SiO_2 substrates by magnetron sputtering. Pure argon gas was used as working gas (p=5×10^{-3} mbar) and the Co target was mounted on a DC power

supply (P=50 W). The distance between the target and the sample stage was about 7 cm and the deposition rate was 2 Å/s. The thermal annealing treatments were performed in a tube furnace in vacuum or in oxidizing atmosphere (air or O_2 flux), at selected temperatures, in the range 200-500 °C. In case of Si substrate, it is known that the native silicon oxide layer, that was not removed prior to Co deposition, does not grow significantly for thermal treatments below T = 500 °C [33]. Moreover, it does not prevent the electrical current flow [34]. The surface roughness and the thickness of the deposited films were measured by a NT-MDT Atomic Force Microscopy (AFM). The total Co fluence was measured by Rutherford Backscattering Spectrometry (RBS).

Field Emission Scanning Electron Microscopy (FE-SEM) was performed with a Zeiss Sigma HD field emission FE-SEM, equipped with InLens, Secondary Electrons (SE) and Backscattered Electrons (BSE) detectors.

Grazing Incidence X-ray Diffraction (GIXRD) experiments were performed by a Panalytical X'Pert Plus diffractometer, using Cu K_α radiation.

The X-ray Absorption Spectroscopy (XAS) experiment was performed in fluorescence mode at 80 K at the Co K-edge at the Italian Beamline LISA-BM08 of the European Synchrotron-ESRF [35]. The XAS spectra of crystalline powder pellets of Co_3O_4, CoO and the spectrum of a Co foil were collected in transmission mode as suitable references. The analysis of the XANES (X-ray Absorption Near-Edge Spectroscopy) spectra was performed with a linear combination fit of the CoO, Co_3O_4 spectra and of the spectrum of an as-deposited metallic Co film. The EXAFS (Extended X-ray Absorption Fine Structure) analysis was performed with the FEFF8-IFEFFIT package [36].

The photoelectrochemical (PEC) measurements were performed at room temperature in a Teflon PEC cell (PINE Research Instrumentation). The Si-Co_3O_4 nanopetal samples were exposed to the solution using a 6 mm diameter o-ring. In this way, the Co_3O_4 mass effectively at work for the PEC experiment resulted about 25 μg. The sample was electrically contacted by pressing a metallic tip on the back side, where a 100 nm-thick Cr-Au contact was preliminary deposited by PVD. A Pt wire and a Ag/AgCl electrode (V = 0.227 V vs Reference Hydrogen Electrode, RHE) were used as counter and reference electrodes, respectively. Illumination in the visible range was performed using a 100 mW/cm^2 LED source (neutral white, Philips LUMILEDS), coupled to an Autolab PGSTAT204 instrument. The experiment was conducted in a sodium phosphate buffer solution (PBS) (50 mM, pH 7, volume = 50 ml). Fenitrothion (FNT, Reference Material from Sigma-Aldrich) was dissolved in acetonitrile with concentration 10 mM. Prior to the sensing experiment, the sample was cycled few times within the used potential range until a stable cyclic voltammetry curve was obtained. Basically, identical CVs were obtained in Ar/purged or air exposed electrolyte. The sensing measurements were performed in a leak-tight cell that was periodically opened to allow the addition of aliquots of 50 μL to the PBS solution. After each addition, the solution was stirred for 5 min, and then the cyclic voltammetry curve was measured for 5 cycles, at a scan rate = 40 mV/s. The addition of each aliquot corresponds to an increase of the FNT concentration in the PBS solution by about 10 μM. The experiment to measure

the FNT degradation was performed after the sensing experiment with the same PEC equipment, starting from a 270 μM solution of FNT in PBS. After stirring to establish the solution/electrode equilibrium, the photoelectrode was polarized at V = 1.45 V vs RHE and illuminated. 0.5 mL of solution was collected after a definite time interval (15 min) and the corresponding UV-Vis optical absorption spectrum was recorded using a Cary 60 Agilent spectrophotometer and normalized to the buffer solution.

Fluorescence measurements were performed with a FLS 1000 fluorimeter (Edinburgh Instruments). The spectra were collected using a quartz cuvette of 1 cm path length. The excitation wavelength was 332 nm and the spectra were collected from 342 to 700 nm. The excitation bandwidth was 1.5 nm, the emission bandwidth was 2.5 nm. Mass spectrometry (MS) experiments were performed with a LC-MS system equipped with an Ultimate 3000 UHPLC chromatograph coupled with a QExactive™ hybrid quadrupole-Orbitrap™ mass spectrometer (Thermo Fisher Scientific). The chromatographic separation was performed by a Kinetex 2.6 µm EVO C18, 100 A, 100x2.1 mm (Phenomenex) column at 40°C and flow rate 0.25 mL/min. The MS analysis was performed in both positive and negative ionization mode, while tandem mass spectra (MS/MS) were acquired in Parallel Reaction Monitoring (PRM) mode.

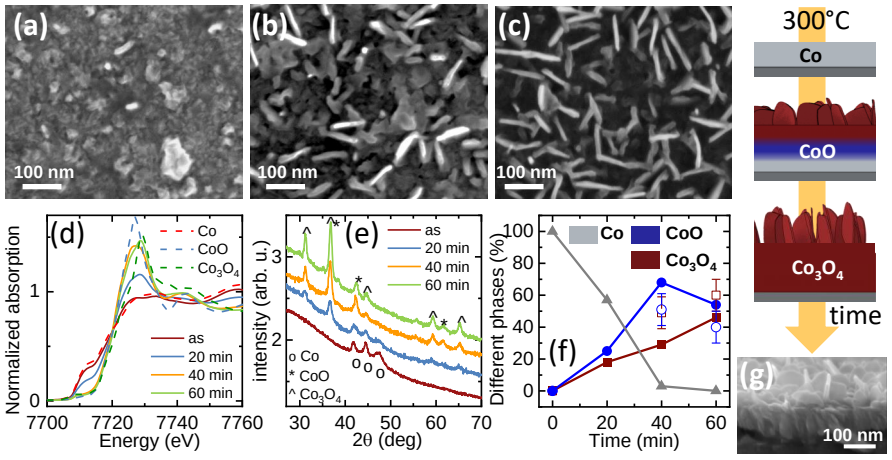

Figure 1: (a-c) SEM images of a 50 nm-thick Co deposited film annealed in air at 300 °C for 20 min (a), 40 min (b) and 60 min (c). (d) XANES spectra (normalized to the K-edge jump) and (e) GIXRD patterns of the same films. (f) Percentage of the different phases, as from XANES analysis. The results from GIXRD are also shown (incidence angle = 1 deg). A sketch of the sample modification during annealing is drawn. The color code is the same as in (f). (g) SEM image of a nanopetal layer (tilted view) obtained from complete oxidation of a 50 nm Co film.

3. Results and discussion

3.1. Nanopetal formation mechanism

To elucidate the formation mechanism of Co_3O_4 nanopetals by oxidation of a thin metallic Co film, we have investigated the film morphology and the structure (atomic site and crystalline phases) after air-annealing at T = 300°C for definite time intervals, corresponding to the initial stages of the petal formation (see Figure 1). As a case study, a 50 nm-thick film has been considered, but the obtained results are valid for all the investigated thicknesses (20-200 nm) and for both silica and Si substrates. The annealing in oxidizing atmosphere promotes an increase of the surface roughness (from less than 1 nm for the as-deposited film to 10±1 nm for the 20-min annealed one, as from AFM analysis), as well as the progressive formation of nanopetals, i.e., platelets less than 10-nm thick and about 150 nm large, grown with the main face almost perpendicular to the original film surface (well visible after 60 min annealing, see Figure 1(c) and Figure 1(g)). In this case, the petal distribution results homogeneous on the whole deposited film surface and from SEM analysis we estimate an average nanopetal density of ≈ 160 nanopetals/μm^2, corresponding to an increased surface area of about 7 times with respect to a flat film.

For a definite annealing condition, the average petal size depends on the original film thickness (thicker films lead to larger petals), while the petal thickness remains always below 10 nm (see Figure S1). The nanopetal layer is easy to be produced, offer a strongly increased surface area useful for catalysis, also combining an optimum stability in working conditions, as discussed in the following. Our results are compatible with others previously reported [24, 25, 26, 27], and extend the range for the nanopetal formation down to very low film thicknesses (20 nm, see Figure S1). A lower thickness of this layer obviously corresponds to a lower optical absorbance (especially in the spectral range above the Co_3O_4 energy gap, i.e. E_g= 1.54 eV [37]) and this is useful in the case where shining the substrate is of interest, as for example when Co nanopetals have to be coupled to Si photoanodes [21, 23].

The XANES and GIXRD signals recorded at different annealing times are reported in Figure 1(d,e), together with the relative fraction of the different phases (f). The analyses show that the Co film progressively oxidizes to CoO (ICSD card 29049) and Co_3O_4 (ICSD card 28058); the Co metallic phase is negligible after 40 min, condition in which the nanopetals are almost completely formed. The complete CoO to Co_3O_4 oxidation occurs after 4-5 hours in a 50 nm-thick film. A GIXRD analysis at different grazing incidence angles indicates that Co_3O_4 is located closer to the external surface with respect to CoO (see Figure S2). The EXAFS analysis on the same films (see Supplementary Information) has been performed considering the local environment around Co atoms in a radius up to 3.5 Å. In agreement with XANES analysis, EXAFS detects a local environment compatible with a combination of CoO, Co_3O_4 and metallic Co. The EXAFS results indicate the presence of a high structural disorder especially for the CoO phase after 1 h annealing, as expected considering the moderate annealing temperature [38] and the fact that CoO is a temporary phase formed

during the oxidation of Co to Co_3O_4. To this respect, it is interesting to note that at higher temperature (700°C) a disordered oxide lattice can induce Co out-diffusion during CoO to Co_3O_4 oxidation [29]. Indeed, also in the present case, as shown in the following, the petals formation is related to Co out-diffusion. A sketch of the structural evolution of the film during oxidation, resulting from this analysis, is shown in Figure 1.

The mechanism for Co_3O_4 petal formation from a Co film at T = 300 °C

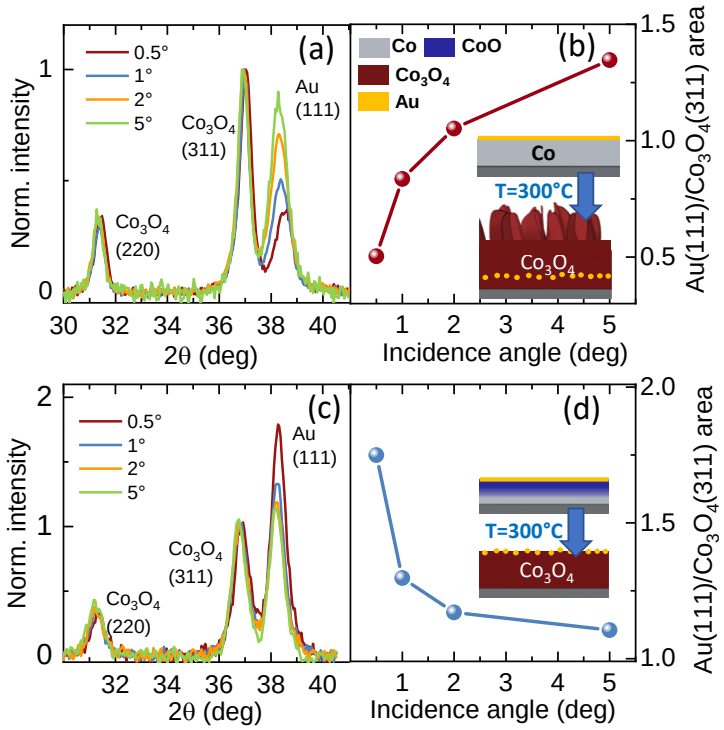

Figure 2: (a) GIXRD spectra recorded at selected incidence angles after heating in oxidizing atmosphere (300°C, 18 h) of a 50 nm Co film capped with a 5 nm Au layer and (b) relative intensity of the Au (111) peak with respect to the Co_3O_4 (311) one. The longer is the penetration depth of the x-ray beam, the more intense is the Au signal with respect to the Co_3O_4 one, indicating that after the annealing the Au clusters are buried in the Co_3O_4 layer. (c) GIXRD spectra recorded at selected incidence angles of a Co film pre-treated in vacuum (500 °C, 1h), then capped with a 5 nm thick Au layer and after heated in oxidizing atmosphere (300°C, 18 h). (d) relative Au/Co_3O_4 peak intensity as in (b), showing that in this case the Au clusters remain on the sample surface. The color code of the sketch is the same as in (b).

is debated in literature. It has been tentatively explained as a sort of Solid-Liquid-Solid (SLS) mechanism, that should start with the melting of a very

thin surface layer of Co (or CoO). Part of oxygen from the annealing atmosphere should then dissolve in this melt and, once the saturation is achieved, the Co-oxide would precipitate in form of Co_3O_4 nanopetals [28, 24]. The fact that the petal formation occurs in a limited range of temperature (300-450°C, see Ref 24, 25, 26, 27) suggests that at least two competitive phenomena enter into play during oxidation, whose combined effect depends on the temperature and on the annealing atmosphere.

Indeed, we show in the following that, besides oxygen diffusion in the film, Co out-diffusion plays a relevant role in the petals formation. To this purpose, a 5 nm-thick Au film was deposited on top of the metallic Co film, preliminary to the oxidizing annealing. Au is intended here to be used as a marker of the original surface. The Au deposition with this low thickness undergoes dewetting during annealing, forming nanometric spheroidal clusters. Moreover, at the modest temperature used, Au does not diffuse appreciably into the Co film, so that, in case of Co out-diffusion during the thermal annealing, Au clusters will be found embedded in the film. It is found that the Au presence does not change the nanopetal formation upon annealing. Indeed, the oxidizing annealing promotes the formation of Co_3O_4 nanopetals whose morphology is the same with or without the Au deposition, ruling out any possible catalytic effect of Au on the Co_3O_4 formation. Nevertheless, the Au clusters remain embedded in the Co_3O_4 layer. Indeed, the GIXRD patterns recorded at increasing incidence angles (Figure 2(a,b)) show that the Au signal is more intense with respect to the Co_3O_4 one when a higher thickness is probed (i.e., when a higher incidence angle is used). This indicates that during heating, Co atoms out-diffuse and form Co_3O_4, so that the original film surface remains embedded in the oxide film. Coherently with this picture, if Au is deposited on top of the completely formed nanopetal layer and then annealed, it remains on the surface, as testified by SEM and GIXRD analysis (not shown).

A completely different scenario comes out if the metallic Co film is pre-treated in vacuum (500°C, 1h, p = 10^{-3} mbar): the formation of a CoO surface layer is indeed detected (involving about 30% of Co atoms, as from XANES analysis, see Figure 3(a)). In this case the subsequent oxidation process takes a longer time, due to the passivating effect of the CoO. Anyway, after 18 h at 300 °C in oxidizing atmosphere, the film is completely oxidized to Co_3O_4 (see Supplementary Information for EXAFS analysis), but the rough surface that results has no petals, see Figure 3(a). Moreover, if a thin Au film is deposited on top of the sample just after the vacuum annealing and before the oxidizing one, the most part of the Au clusters remain on the external surface, as shown by GIXRD (see Figure 2(c,d)).

These results indicate that the petal formation is related to the out-diffusion of Co through the film surface. If this process is inhibited (as in case of Figures 2(c) and 3(a)), no petals are formed. Out-diffusion of Co has been demonstrated at higher temperature during oxidation of Co-O-B nanoparticles (T=500 °C) [39] and also of bulk phases (Co to CoO at T$\geq$ 1000 °C, [40] and CoO to Co_3O_4 at T$\geq$ 700 °C[29]). In this last case in particular, the oxidation process was shown to depend on Co out-diffusion through the oxide induced by a gradient of cation

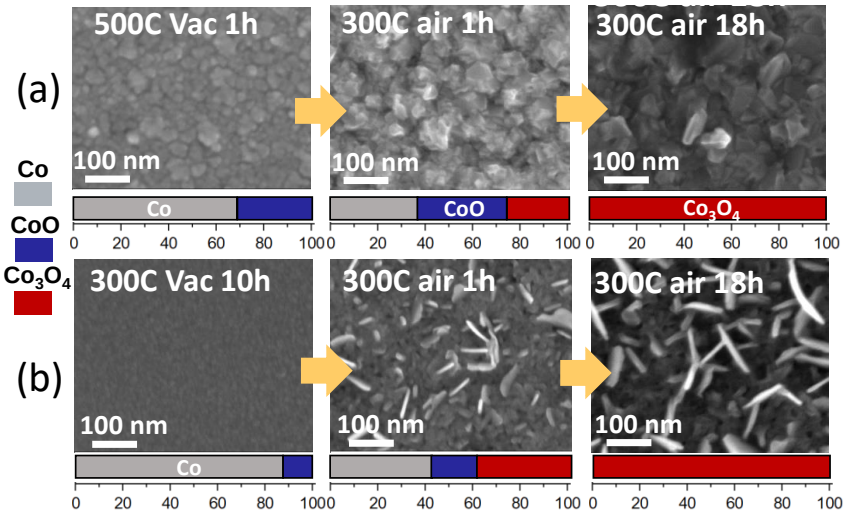

Figure 3: Surface morphology from SEM (top view) as obtained by 300 °C air annealing on a 50-nm thick Co film pre-treated in vacuum (a) at 500 °C for 1h or (b) at 300 °C for 10 h. The percentage of the different phases as from Co K-edge XANES analysis is reported. In the first case (a) the petal formation process is inhibited, in the second one (b) it is slower than without the vacuum annealing (see Figure 1(a-c) for comparison).

vacancies in the oxide spinel lattice. Moreover, it has been shown that at lower temperature (about 200 °C), metallic Co nanoparticles can be oxidized to hollow CoO spheroidal particles, with a nanoscale Kirkendall-like effect, in which Co out-diffusion occurs more rapidly than inward oxygen diffusion [30, 31]. A very similar process seems to occur here, where at 300 °C Co out-diffusion coexists with inward oxygen diffusion. The nanostructured character of the thin film and the non-stoichiometric oxides present at the moderate temperature used for the annealing favor the presence of defects and the formation of fast diffusion channels for Co, that determine a spatially non-homogeneous out-diffusion rate. That is, the out-diffusion of Co promotes a fast oxidation, and its partially non-uniform character due to grain boundaries and surface defects induces the nanopetals formation. In the case of the film pre-treated in vacuum, the higher temperature used (500 °C) leads to a more compact and less defective CoO surface layer, that, during the T = 300 °C oxidizing annealing, inhibits the Co out-diffusion and the petal formation. Nevertheless, in both cases, oxygen diffuses into the film and promotes Co oxidation to Co_3O_4. A further element that corroborate this phenomenological model is the analysis of a Co film pre-treated in vacuum at lower temperature (300°C, 10 h) and then heated in air. The vacuum annealing in this case determines the formation of a thinner CoO layer (involving about 15% of Co atoms), with respect to the vacuum annealing

at T = 500 °C. The subsequent air annealing induces the formation of Co_3O_4 nanopetals (Figure 3(b)), although through a slower out-diffusion process than in the case without the vacuum pre-annealing (Figure 1(c)). Anyway, after 18 h in air at 300 °C, the surface morphology of the two films results very similar. This is indeed an intermediate situation with respect to the previous two, with a thin passivating layer that slows down the non-uniform Co out-diffusion without completely stopping it.

The obtained results indicate that the mechanism for the Co_3O_4 nanopetal formation proposed in literature does not seem to work in the present system. Indeed, when nanopetals form, an oxidized surface layer is already formed (see for example the film annealed for 20 min at 300 °C in air, Figure 1). Moreover, a CoO surface layer can or cannot inhibit the petal formation upon a subsequent air annealing (Figure 3), depending on the temperature used for its formation. In addition, Co oxidation upon annealing involves out-diffusion of Co atoms, with the formation of an oxide layer out of the pristine surface, as demonstrated by Au markers. This oxide layer, depending on the annealing conditions, can have fast diffusion channels for Co, that induce the petals formation if there is a metallic layer beneath. Indeed, no petal formation is observed if the metallic film is first completely oxidized to CoO. The role of the metallic layer is crucial, likely because it maintains a gradient of Co concentration through the oxide layer [29], essential for Co out-diffusion. Finally, in agreement with previous results [24, 25, 27], we also find that Co_3O_4 nanopetals form upon Co oxidation only in the temperature range 300-450 °C. We suggest that in this temperature range a subtle equilibrium is reached, in which the oxygen diffusion into the film does not overwhelm Co out-diffusion. At the same time the defective surface layer makes this last process spatially non-uniform and the Co_3O_4 nanopetals grow. In Figure 4 the process of the Co_3O_4 nanopetal formation is summarized. So, the results of the performed experiments clarify the diffusion-driven formation character of the Co_3O_4 nanopetals. This simple, cost-effective and relatively low-temperature synthesis procedure, based on physical vapor deposition and subsequent oxidizing annealing, allows to obtain stable Co_3O_4 nanopetal layers, whose extended surface makes them very promising for catalytic applications, as demonstrated in the following section.

3.2. FNT photoelectrochemical sensing and degradation

In the following, we show how a small amount of Co_3O_4 nanopetals grown on n-Si can effectively detects and degrades FNT, a major OP pesticide. A completely oxidized Co_3O_4 layer has been used in this case (annealing for 4h at 300 °C+ 4h at 350 °C in O_2). The n-Si/SiO_x/Co_3O_4 nanopetal system produced for this experiment will be labelled 'Si-Co_3O_4' hereafter. While the electrochemical detection of FNT is usually obtained by the chemical reduction of the nitro-group to hydroxylamino group [12], here we show a novel sensing scheme that can be applied directly using the Si-Co_3O_4 as photoanodes. For the photoelectrochemical sensing, the role of the formed nanopetal layer is crucial to obtain a significant photocurrent, mandatory for a reliable sensing signal. In Figure 5(a) the cyclic voltammetry (CV) measurement for a Si-Co_3O_4 nanopetal

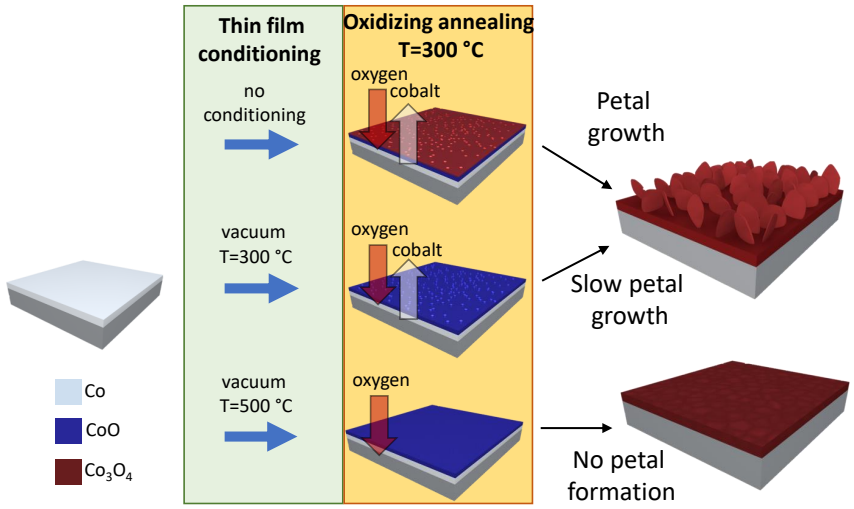

Figure 4: Sketch of the Co_3O_4 petal formation process by oxidizing annealing of a metallic film, as obtained from the presented experiments.

layer in 0.05 M PBS solution at pH 7.0 is compared to the one obtained for a Si-Co_3O_4 layer without nanopetals (i.e., see SEM picture in Figure 3(a)) and with/without illumination. Consistently with the estimated increased surface area related to the Co_3O_4 nanopetals, a ∼5 times higher current density is observed especially under illumination, due to the migration of the holes photogenerated in Si towards the Co_3O_4 surface. The peak in the range 1.4-1.5 V is also strongly enhanced under illumination by the presence of nanopetals and corresponds to the Co(II) → Co(III) oxidation with formation, in neutral or alkaline solution, of CoO(OH), as previously reported [41], while the corresponding inverse reaction occurs in the range 1.1-1.3 V [42]. It is worth noting that the anodic peak corresponding to the Co(III)/Co(IV) oxidation is not visible in the CV scans because of the very steep photocurrent increase starting from V = 1.5 V. The Incident Photon to Current Efficiency (IPCE) spectra acquired close to the working condition and reported in Figure S4 show that the efficiency of the nanopetal layer, comparable with other similar nanostructured systems [43], is much higher than for the layer without nanopetals in the whole spectral region explored, in agreement with the CV curves. The evolution of the CV curves, measured under illumination upon a progressive increase of the FNT concentration is shown in Figure 5(b). It is found that the values of the current intensity of the anodic (at 1.45 V) and cathodic (at 1.2 V) peaks gradually decrease with the FNT concentration. This remarkable decrease of the peak current is explained by the coordination of nitro-group of the FNT on

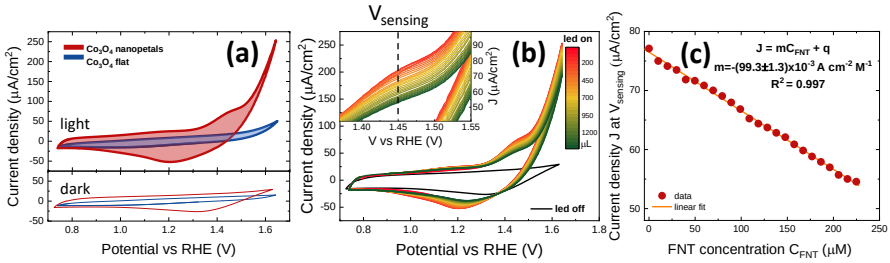

Figure 5: (a) Cyclic voltammetry curves for a Si-Co_3O_4 nanopetal layer and for a Si-Co_3O_4 flat layer, measured in 0.05 M PBS (pH = 7.0) in dark and under visible illumination. (b) Cyclic voltammetry curves in 0.05 M PBS (pH = 7.0) recorded under white illumination with successive additions of 50 µL of 10 mM solution of FNT. The inset shows a magnification in the region of the anodic peak, related to the Co(II) → Co(III) oxidation with formation of CoO(OH). The cycle recorded in dark condition before the FNT addition is also reported (black curve). (c) Current density measured at V = 1.45 V vs RHE, obtained from the CV curves in (b), as a function of the FNT concentration. The linear fit in the 9-200 μM concentration range is shown.

the Co(II) centers, thus suppressing their oxidation to Co(III). The chemisorption of the FNT on the Co(II) sites through the -NO_2 functional group was confirmed by a control experiment, performed by using nitro-benzene (in a similar concentration range). A very similar decrease of the Co(II)/Co(III) peak is recorded (see Figure S5), strongly suggesting that in both cases the nitro-group coordinates on the Co(II) centers of the Co_3O_4 nanopetals. It is worth noting that if, instead, glucose is added, a molecule known to be oxidized on Co(III) and Co(IV) sites [44], a small increase of the Co(II)/Co(III) peak is observed, together with a much more pronounced increase of the photocurrent. The maximum relative variation of the photocurrent, induced by the increase of the FNT concentration is obtained at the Co(II) oxidation peak (V = 1.45 V vs RHE). In Figure 5(c) a plot of the photocurrent density corresponding to the maximum of the anodic peak is shown as a function of the FNT concentration. A linear trend is found in a wide concentration range of FNT, up to at least 200 μM, with a good sensitivity of $(100 \pm 1)\text{x}10^{-3}$ μA/(cm$^2\mu$M). It is worth to point out that, in this case, the photoelectrochemical detection of FNT relies on a "negative" response, in terms of photocurrent, since FNT cannot work as a hole scavenger, but shades the Co(II)/Co(III) and Co(III)/Co(IV) electrocatalytic active sites, so decreasing water oxidation. To the best of our knowledge this is the first example where this working principle is used for FNT detection. Compared to the direct electrochemical detection of FNT based on modified electrodes reported in the literature [12], the photoelectrochemical detection achieved by our Co_3O_4 nanopetals-based sensor revealed higher reusability and robustness with comparable sensitivity. Indeed, the same electrode surface can be used several times with no loss of properties. The same experiment per-

formed on the same electrode after more than 5 h in working conditions shows the same sensitivity within the experimental uncertainty, indicating a very stable and reproducible behavior. Moreover, the sensing process does not modify the electrode permanently. Indeed, the XPS spectra recorded before and after the sensing experiment (see Figure S6) show no difference, apart from a trace of Na on the surface (from the sodium phosphate solution).

The same experimental setup has been used to test the ability of the Si-Co_3O_4

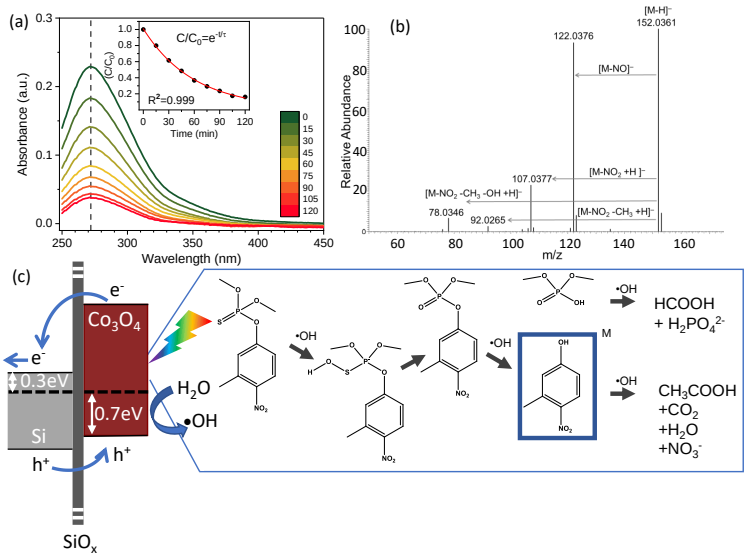

Figure 6: (a) UV-Vis spectra recorded at definite time intervals during the FNT photoelectrodegradation experiment, normalized to the buffer solution. The inset shows the intensity decrease of the peak at λ=270 nm as function of time, superimposed to the best-fit exponential curve. Blue dots indicate the evolution of the normalized absorbance of the peak at λ = 270 nm for the control experiment. (b) Electrospray negative ionization MS/MS spectrum of the degradation product shown in the blue box in (c). M stands for molecular weight of the FNT intermediate (all signals are referred to negative ions). Data acquired from the FNT-PBS solution after 2 h under illumination (100 mW/cm^2) and bias applied (1.45 V vs RHE). (c) Proposed electronic band diagram for Si-Co_3O_4 nanopetal layer and degradation pathway of FNT over the Co_3O_4 nanopetals.

nanopetals to degrade the FNT through the generation of hydroxyl radicals under visible light irradiation. First of all, the generation of hydroxyl radicals by our Si-Co_3O_4 nanopetals was evaluated under irradiation with visible light and the application of 1.5 V vs RHE at the working electrode (the Pt counter electrode was separated by a glass frit) in a PBS solution containing 1 mM coumarin, which is usually employed as fluorescent probe to detect OH radicals

[45, 46]. After the flow of a 1.1 C of charge in the circuit, we measured a strong emission spectra centered at 456 nm (Figure S8), corresponding to the formation of 7-hydroxycoumarin and confirming the generation of hydroxyl radicals, as also reported for similar systems [47]. The OH radical generation is induced by the photogenerated holes in the material that reach the solution. To this respect, is interesting to consider the electronic energy diagram of the composite material. The XPS analysis of the valence band of the Co_3O_4 nanopetal layer indicates that the Fermi level is about 0.7 eV above the valence band. The n-Si Fermi level, estimated from the Si doping condition, is about 0.3 eV below the conduction band. Moreover, the energy gap of the Co_3O_4 nanopetal layer (measured from a Tauc plot of a layer grown in the same conditions on a soda-lime glass slide) is about 2.2 eV, in agreement with literature [48]. Considering these data and the energy gap of Si, the electronic band structure of the system can be schematically represented as in Figure 6(c), showing that the holes photogenerated in Si migrate towards Co_3O_4 where, once in contact with the solution, they generate OH radicals. It is worth noting that, in agreement with previous observation, the Si photoactivity is relevant for the process [49, 34]. This can be seen from the IPCE spectrum of the Si-Co_3O_4 nanopetals (Figure S4), showing that the photon-to-current conversion efficiency is higher in the spectral region where the Co_3O_4 transmittance is higher.

The FNT photodegradation was evaluated on a 270 μM FNT solution in PBS, that was placed in contact with the electrode under illumination (100 mW/cm^2) and with an applied bias (V=1.45 V). In Figure 6(a) the absorption spectrum of the prepared solution is reported, showing the absorption band at about 270 nm related to the aromatic ring present in the FNT molecule [12]. A decrease of the intensity of the absorption band is observed with the irradiation time, indicating that the FNT molecule decomposes through the action of hydroxyl radicals. The results of the mass spectrometry (MS), performed after 2 h of irradiation, are shown in Figure 6(b) and indicate that the FNT decomposes through the intermediate 3-methyl-4-nitro-phenol (MW: 153.0426, labelled 'M' in Figure 6(c)). According to the previous observations, after 2 h of irradiation about 20% of FNT is left in solution together with a small quantity of 3-methyl-4-nitrophenol, that is then further decomposed to CO_2 through the action of hydroxyl radicals, following a first order kinetic [50]. In agreement with this, the maximum of the absorption spectrum shows an exponential decay with a time constant τ=(59 $\pm$ 3) min, as reported in the inset of Figure 6(a). A control experiment was performed to evaluate the FNT stability upon white light illumination (P=100 mW/cm^2, same condition as above) without the Si-Co_3O_4 electrode (replaced by a silica window). No decrease of the FNT absorbance peak at λ=270 nm was detected (see inset Figure 6(a) and Figure S9(a)), demonstrating that the FNT degradation reported in 6(a) is due to the catalytic action of the Si-Co_3O_4 nanopetals electrode. The LED source used, indeed, does not emit in the UV spectral range and therefore there is no overlap between the emission spectrum of the light source and the absorbance spectrum of the FNT, see Figure S9(b). Considering the overall process, the visible light is absorbed by the Si and by Co_3O_4 nanopetal layer. The photogenerated holes

are driven in solution, promoting OH radical generation that initiate the degradation reaction. A possible degradation pathway of the FNT, suggested by the experimental results, is proposed in Figure 6(c).

The results presented show that the Si-Co_3O_4 systems operated as photoanodes can effectively detect and degradate FNT, and remain stable after intensive and repeated use, as shown by the SEM images of the nanopetal surface Figure S6(b,c) and by the XRD spectra (Figure S7) recorded before and after use (about 10 h, considering all the tests and experiments). It is worth noting that, although in our case a moderate bias is needed, the process works with visible light, i.e., with no need for UV radiation. Recent literature reports different examples where photocatalysts efficiently degrade organophosphate pesticides [51, 52, 12], normally upon UV-irradiation. For photocatalysts based on TiO_2 [51, 52] or Ti-Fe mixed oxide [53], the ratio between the mass of pesticides over the mass of catalyst needed to degrade the pesticide in about 1 h was in the range 3-6%. UV-irradiated powders of Gd-based nanoflowers [51] were also effective for FNT degradation in a similar time scale, with a pesticide/catalyst mass ratio higher than 15 [12]. FNT degradation has been also demonstrated by Fe-activated persulfate, with promising results restricted to acidic conditions [50]. The direct comparison between literature results with those presented here is not straightforward, due to the different spectral illumination. Nevertheless, in our case a very small quantity of catalyst is needed (to degrade about 3 mg of FNT about 25 μg of Co_3O_4, corresponding to about 8/1000 mass ratio) and there is no need for further filtering to gather the dispersed catalyst at the end of the process. This makes the investigated Co_3O_4-nanopetal system a very effective platform for water remediation from organophosphate pesticides like FNT.

4. Conclusions

We have demonstrated how wide-area, stable and effective Co_3O_4 nanopetals grow in a controllable way on Si wafers and glass substrates. The mechanism of Co_3O_4 nanopetals formation has been addressed, combining morphological and structural analysis of the films after specific annealing conditions. We have shown that the petal formation is a mechanism induced by out-diffusion of Co atoms from the original film surface, rather than by a local melting, followed by subsequent oxidation. The results presented clarify that the petal formation requires a subtle equilibrium between the oxygen diffusion into the film and the non-uniform out-diffusion of Co atoms from the metallic film. Coupled to n-Si, Co_3O_4 nanopetals constitute an efficient photoanode for the photoelectrochemical detection of the organophosphate pesticide FNT, showing good sensitivity in a wide linear range, reproducibility and stability. The Si-Co_3O_4 nanopetals system also works very effectively for water remediation from organophosphate pesticides like FNT. Indeed, the production of hydroxyl radicals in a phosphate buffer solution, under visible light illumination, leads to a pesticide decomposition with a characteristic time of 1 h. This system can be used several times, showing an excellent stability under working conditions, without any significant

morphological or compositional surface change. These positive features, obtained with materials whose supply risk is at present not critical, and especially without using nanopowders, make this system highly promising for practical applications in contaminated water treatment.

Acknowledgements

We acknowledge Francesco D'Acapito (BM08 beamline at ESRF, CNR-IOM) for assistance during measurements, the European Synchrotron Radiation Facility (BM08 beamline) and the Italian National Research Council (CNR) for provision of beamtime. M.F. and R.B. acknowledge support from the project "AMICO" funded by the MIUR PRIN 2017 (Project n. 2017EZNJWN). The research has been funded by the projects HILIGHT (SID_2017) and FUN-FACE (SID_2019) of the Physics and Astronomy Department (UNIPD). This work was partially supported by the following projects: the Italian MIUR (PRIN2017: Multi-e, No. 20179337R7) and CNR (Progetti di Ricerca @CNR – avviso 2020 – ASSIST).

References

[1] M. Arias-Estévez, E. López-Periago, E. Martínez-Carballo, J. Simal-Gándara, J.-C. Mejuto, L. García-Río, The mobility and degradation of pesticides in soils and the pollution of groundwater resources, Agriculture, Ecosystems & Environment 123 (4) (2008) 247–260. doi:10.1016/j.agee.2007.07.011.

[2] G. Aragay, F. Pino, A. Merkoçi, Nanomaterials for sensing and destroying pesticides, Chemical Reviews 112 (10) (2012) 5317–5338. doi:10.1021/cr300020c.

[3] T. Maric, M. Z. M. Nasir, C. C. Mayorga-Martinez, N. F. Rosli, M. Budanović, K. Szőkölová, R. D. Webster, Z. Sofer, M. Pumera, Cloisite microrobots as self-propelling cleaners for fast and efficient removal of improvised organophosphate nerve agents, ACS Applied Materials & Interfaces 11 (35) (2019) 31832–31843, pMID: 31433151. doi:10.1021/acsami.9b08332.

[4] D. Capoferri, R. Álvarez Diduk, M. Del Carlo, D. Compagnone, A. Merkoçi, Electrochromic molecular imprinting sensor for visual and smartphone-based detections, Analytical Chemistry 90 (9) (2018) 5850–5856. doi:10.1021/acs.analchem.8b00389.

[5] X. Lian, B. Yan, Trace detection of organophosphorus chemical warfare agents in wastewater and plants by luminescent UIO-67(Hf) and evaluating the bioaccumulation of organophosphorus chemical warfare agents, ACS Applied Materials & Interfaces 10 (17) (2018) 14869–14876. doi:10.1021/acsami.8b00289.

[6] C.-H. Hao, X.-N. Guo, M. Sankar, H. Yang, B. Ma, Y.-F. Zhang, X.-L. Tong, G.-Q. Jin, X.-Y. Guo, Synergistic effect of segregated Pd and Au nanoparticles on semiconducting SiC for efficient photocatalytic hydrogenation of nitroarenes, ACS Applied Materials & Interfaces 10 (27) (2018) 23029–23036. doi:10.1021/acsami.8b04044.

[7] D. Ayodhya, G. Veerabhadram, Ternary semiconductor $Zn_xAg_{1x}S$ nanocomposites for efficient photocatalytic degradation of organophosphorus pesticides, Photochem. Photobiol. Sci. 17 (2018) 1429–1442. doi:10.1039/C8PP00220G.

[8] K. O. Kirlikovali, Z. Chen, T. Islamoglu, J. T. Hupp, O. K. Farha, Zirconium-based metal–organic frameworks for the catalytic hydrolysis of organophosphorus nerve agents, ACS Applied Materials & Interfaces 12 (13) (2020) 14702–14720. doi:10.1021/acsami.9b20154.

[9] R. Ricco, M. J. Styles, P. Falcaro, MOF-based devices for detection and removal of environmental pollutants, in: S. K. Ghosh (Ed.), Metal-Organic Frameworks (MOFs) for Environmental Applications, Elsevier, 2019, pp. 383–426. doi:10.1016/B978-0-12-814633-0.00012-0.

[10] Y. Huang, Y. Lu, Y. Lin, Y. Mao, G. Ouyang, H. Liu, S. Zhang, Y. Tong, Cerium-based hybrid nanorods for synergetic photo-thermocatalytic degradation of organic pollutants, J. Mater. Chem. A 6 (2018) 24740–24747. doi:10.1039/C8TA06565A.

[11] Y. Huang, Z. Guo, H. Liu, S. Zhang, P. Wang, J. Lu, Y. Tong, Heterojunction architecture of N-doped WO_3 nanobundles with Ce_2S_3 nanodots hybridized on a carbon textile enables a highly efficient flexible photocatalyst, Advanced Functional Materials 29 (45) (2019) 1903490. doi:10.1002/adfm.201903490.

[12] J. Vinoth Kumar, R. Karthik, S.-M. Chen, K. Natarajan, C. Karuppiah, C.-C. Yang, V. Muthuraj, 3D flower-like gadolinium molybdate catalyst for efficient detection and degradation of organophosphate pesticide (fenitrothion), ACS Applied Materials & Interfaces 10 (18) (2018) 15652–15664. doi:10.1021/acsami.8b00625.

[13] X. Xie, W. Shen, Morphology control of cobalt oxide nanocrystals for promoting their catalytic performance, Nanoscale 1 (2009) 50–60. doi:10.1039/B9NR00155G.

[14] X. Ma, S. Feng, L. He, M. Yan, X. Tian, Y. Li, C. Tang, X. Hong, L. Mai, Rapid, all dry microfabrication of three-dimensional Co_3O_4/Pt nanonetworks for high-performance microsupercapacitors, Nanoscale 9 (2017) 11765–11772. doi:10.1039/C7NR01789H.

[15] Y. Ding, Y. Wang, L. Su, M. Bellagamba, H. Zhang, Y. Lei, Electrospun Co_3O_4 nanofibers for sensitive and selective glucose detection, Biosensors

and Bioelectronics 26 (2) (2010) 542 – 548. doi:10.1016/j.bios.2010.07.050.

[16] S. F. Shen, M. L. Xu, D. B. Lin, H. B. Pan, The growth of urchin-like Co_3O_4 directly on sensor substrate and its gas sensing properties, Applied Surface Science 396 (2017) 327–332. doi:10.1016/j.apsusc.2016.10.147.

[17] P-type Co_3O_4 nanomaterials-based gas sensor: Preparation and acetone sensing performance, Sensors and Actuators B: Chemical 242 (2017) 369–377. doi:10.1016/j.snb.2016.11.067.

[18] P. G. Choi, T. Fuchigami, K.-i. Kakimoto, Y. Masuda, Effect of crystal defect on gas sensing properties of Co_3O_4 nanoparticles, ACS Sensors 5 (6) (2020) 1665–1673. doi:10.1021/acssensors.0c00290.

[19] J. Wang, R. Gao, D. Zhou, Z. Chen, Z. Wu, G. Schumacher, Z. Hu, X. Liu, Boosting the electrocatalytic activity of Co_3O_4 nanosheets for a Li-O_2 battery through modulating inner oxygen vacancy and exterior Co^{3+}/Co^{2+} ratio, ACS Catalysis 7 (10) (2017) 6533–6541. doi:10.1021/acscatal.7b02313.

[20] R. Edla, N. Patel, M. Orlandi, N. Bazzanella, V. Bello, C. Maurizio, G. Mattei, P. Mazzoldi, A. Miotello, Highly photo-catalytically active hierarchical 3D porous/urchin nanostructured Co_3O_4 coating synthesized by pulsed laser deposition, Applied Catalysis B: Environmental 166-167 (2015) 475 – 484. doi:10.1016/j.apcatb.2014.11.060.

[21] S. A. Lee, T. H. Lee, C. Kim, M.-J. Choi, H. Park, S. Choi, J. Lee, J. Oh, S. Y. Kim, H. W. Jang, Amorphous Cobalt Oxide Nanowalls as Catalyst and Protection Layers on n-Type Silicon for Efficient Photoelectrochemical Water Oxidation, ACS Catalysis 10 (1) (2020) 420–429. doi:10.1021/acscatal.9b03899.

[22] J. Zhang, X. Chang, Z. Luo, T. Wang, J. Gong, A highly efficient photoelectrochemical H_2O_2 production reaction with Co_3O_4 as a co-catalyst, Chem. Commun. 54 (2018) 7026–7029. doi:10.1039/C8CC03303J.

[23] L. Girardi, L. Bardini, N. Michieli, B. Kalinic, C. Maurizio, G. A. Rizzi, G. Mattei, Co_3O_4 nanopetals on Si as photoanodes for the oxidation of organics, Surfaces 2 (1) (2019) 41–53. doi:10.3390/surfaces2010004.

[24] B. Varghese, C. Teo, Y. Zhu, M. Reddy, B. Chowdari, A. Wee, V. Tan, C. Lim, C.-H. Sow, Co_3O_4 nanostructures with different morphologies and their field-emission properties, Advanced Functional Materials 17 (12) (2007) 1932–1939. doi:10.1002/adfm.200700038.

[25] L. He, Z. Li, Z. Zhang, Rapid, low-temperature synthesis of single-crystalline Co_3O_4 nanorods on silicon substrates on a large scale, Nanotechnology 19 (15) (2008) 155606. doi:10.1088/0957-4484/19/15/155606.

[26] Y. Sun, P. Lv, J.-Y. Yang, L. He, J.-C. Nie, X. Liu, Y. Li, Ultrathin Co_3O_4 nanowires with high catalytic oxidation of CO, Chemical Communications 47 (40) (2011) 11279–11281. doi:10.1039/C1CC14484G.

[27] Z. Dong, Y. Fu, Q. Han, Y. Xu, H. Zhang, Synthesis and Physical Properties of Co_3O_4 Nanowires, The Journal of Physical Chemistry C 111 (50) (2007) 18475–18478. doi:10.1021/jp075365l.
URL 10.1021/jp075365l

[28] T. Yu, Y. W. Zhu, X. J. Xu, Z. X. Shen, P. Chen, C.-T. Lim, J. T.-L. Thong, C.-H. Sow, Controlled Growth and Field-Emission Properties of Cobalt Oxide Nanowalls, Advanced Materials 17 (13) (2005) 1595–1599. doi:10.1002/adma.200500322.

[29] A. Kaczmarska, Z. Grzesik, S. Mrowec, On the Defect Structure and Transport Properties of Co_3O_4 Spinel Oxide, High Temperature Materials and Processes 31 (4-5) (2012) 371–379. doi:10.1515/htmp-2012-0069.

[30] Y. Yin, R. M. Rioux, C. K. Erdonmez, S. Hughes, G. A. Somorjai, A. P. Alivisatos, Formation of Hollow Nanocrystals Through the Nanoscale Kirkendall Effect, Science 304 (5671) (2004) 711–714. doi:10.1126/science.1096566.

[31] D.-H. Ha, L. M. Moreau, S. Honrao, R. G. Hennig, R. D. Robinson, The oxidation of cobalt nanoparticles into Kirkendall-hollowed CoO and Co_3O_4: The diffusion mechanisms and atomic structural transformations, The Journal of Physical Chemistry C 117 (27) (2013) 14303–14312. doi:10.1021/jp402939e.

[32] Critical raw materials for strategic technologies and sectors in the EU: a foresight study. https://ec.europa.eu/docsroom/documents/42881, Tech. rep. (2020).

[33] M. Morita, T. Omi, Characterization and control of native oxide on silicon, Jap. J. Appl. Phys. 33 (1994) 370–374. doi:10.1143/JJAP.33.370.

[34] S. Oh, S. Jung, Y. H. Lee, J. T. Song, T. H. Kim, D. K. Nandi, S.-H. Kim, J. Oh, Hole-selective CoO_x/SiO_x/Si heterojunctions for photoelectrochemical water splitting, ACS Catalysis 8 (10) (2018) 9755–9764. doi:10.1021/acscatal.8b03520.

[35] F. d'Acapito, G. O. Lepore, A. Puri, A. Laloni, F. La Manna, E. Dettona, A. De Luisa, A. Martin, The LISA beamline at ESRF, Journal of Synchrotron Radiation 26 (2) (2019) 551–558. doi:10.1107/S160057751801843X.

[36] B. Ravel, M. Newville, ATHENA, ARTEMIS, HEPHAESTUS: data analysis for X-ray absorption spectroscopy using IFEFFIT, Journal of Synchrotron Radiation 12 (4) (2005) 537–541.

[37] L. Qiao, H. Y. Xiao, H. M. Meyer, J. N. Sun, C. M. Rouleau, A. A. Puretzky, D. B. Geohegan, I. N. Ivanov, M. Yoon, W. J. Weber, M. D. Biegalski, Nature of the band gap and origin of the electro-/photo-activity of Co_3O_4, J. Mater. Chem. C 1 (2013) 4628–4633. doi:10.1039/C3TC30861H.

[38] C. Maurizio, N. El Habra, G. Rossetto, M. Merlini, E. Cattaruzza, L. Pandolfo, M. Casarin, XAS and GIXRD study of Co sites in $CoAl_2O_4$ layers grown by MOCVD, Chemistry of Materials 22 (5) (2010) 1933–1942. doi:10.1021/cm9018106.

[39] C. Maurizio, R. Edla, N. Michieli, M. Orlandi, A. Trapananti, G. Mattei, A. Miotello, Two-step growth mechanism of supported Co_3O_4-based sea-urchin like hierarchical nanostructures, Applied Surface Science 439 (2018) 876–882. doi:10.1016/j.apsusc.2018.01.121.

[40] R. Carter, F. Richardson, Oxidation of cobalt metal (1955) 336–343.

[41] F. Reikowski, F. Maroun, I. Pacheco, T. Wiegmann, P. Allongue, J. Stettner, O. M. Magnussen, Operando surface X-ray diffraction studies of structurally defined Co_3O_4 and CoOOH thin films during oxygen evolution, ACS Catalysis 9 (5) (2019) 3811–3821. doi:10.1021/acscatal.8b04823.

[42] The oxidation reaction is shifted here towards a slightly higher potential with respect to the value of the cited reference likely due to the native silicon oxide layer that was not removed prior to the Co deposition. Indeed, all the potentials related to redox events at the Co_3O_4 surface are shifted by about 0.20 - 0.25 V.

[43] S.-S. Yi, B.-R. Wulan, J.-M. Yan, Q. Jiang, Highly efficient photoelectrochemical water splitting: Surface modification of cobalt-phosphate-loaded Co_3O_4/Fe_2O_3 p–n heterojunction nanorod arrays, Advanced Functional Materials 29 (11) (2019) 1801902. doi:https://doi.org/10.1002/adfm.201801902.

[44] Y. Ding, Y. Wang, L. Su, M. Bellagamba, H. Zhang, Y. Lei, Electrospun Co_3O_4 nanofibers for sensitive and selective glucose detection, Biosensors and Bioelectronics 26 (2) (2010) 542–548. doi:10.1016/j.bios.2010.07.050.

[45] H. Czili, A. Horváth, Applicability of coumarin for detecting and measuring hydroxyl radicals generated by photoexcitation of TiO_2 nanoparticles, Applied Catalysis B: Environmental 81 (3-4) (2008) 295–302.

[46] A. D. Proctor, B. M. Bartlett, Hydroxyl radical suppression during photoelectrocatalytic water oxidation on WO_3-FeOOH, The Journal of Physical Chemistry C 124 (33) (2020) 17957–17963.

[47] Y. Wang, C. Zhu, G. Zuo, Y. Guo, W. Xiao, Y. Dai, J. Kong, X. Xu, Y. Zhou, A. Xie, C. Sun, Q. Xian, 0D/2D Co_3O_4/TiO_2 Z-scheme heterojunction for boosted photocatalytic degradation and mechanism investigation, Applied Catalysis B: Environmental 278 (2020) 119298. doi:10.1016/j.apcatb.2020.119298.

[48] D. Barreca, C. Massignan, S. Daolio, M. Fabrizio, C. Piccirillo, L. Armelao, E. Tondello, Composition and Microstructure of Cobalt Oxide Thin Films Obtained from a Novel Cobalt(II) Precursor by Chemical Vapor Deposition, Chemistry of Materials 13 (2) (2001) 588–593. doi:10.1021/cm001041x.

[49] J. Yang, K. Walczak, E. Anzenberg, F. M. Toma, G. Yuan, J. Beeman, A. Schwartzberg, Y. Lin, M. Hettick, A. Javey, J. W. Ager, J. Yano, H. Frei, I. D. Sharp, Efficient and Sustained Photoelectrochemical Water Oxidation by Cobalt Oxide/Silicon Photoanodes with Nanotextured Interfaces, Journal of the American Chemical Society 136 (17) (2014) 6191–6194. doi:10.1021/ja501513t.

[50] H. Liu, J. Yao, L. Wang, X. Wang, R. Qu, Z. Wang, Effective degradation of fenitrothion by zero-valent iron powder (Fe^0) activated persulfate in aqueous solution: Kinetic study and product identification, Chemical Engineering Journal 358 (2019) 1479–1488. doi:10.1016/j.cej.2018.10.153.

[51] P. Kormali, D. Dimoticali, D. Tsipi, A. Hiskia, E. Papaconstantinou, Photolytic and photocatalytic decomposition of fenitrothion by $PW_{12}O_{40}^3$ and TiO_2: a comparative study, Applied Catalysis B: Environmental 48 (3) (2004) 175–183. doi:10.1016/j.apcatb.2003.10.002.

[52] G. R. M. Echavia, F. Matzusawa, N. Negishi, Photocatalytic degradation of organophosphate and phosphonoglycine pesticides using TiO_2 immobilized on silica gel, Chemosphere 76 (5) (2009) 595–600. doi:10.1016/j.chemosphere.2009.04.055.

[53] J. Henych, V. Štengl, M. Slušná, T. Matys Grygar, P. Janoš, P. Kuráň, M. Šťastný, Degradation of organophosphorus pesticide parathion methyl on nanostructured titania-iron mixed oxides, Applied Surface Science 344 (2015) 9–16. doi:10.1016/j.apsusc.2015.02.181.